www.sciencemag.org/cgi/content/full/1165243/DC1

Supporting Online Material for

Strong Release of Methane on Mars in Northern Summer 2003

Michael J. Mumma,* Geronimo L. Villanueva, Robert E. Novak, Tilak Hewagama, Boncho P. Bonev, Michael A. DiSanti, Avi M. Mandell, Michael D. Smith

*To whom correspondence should be addressed. E-mail: michael.j.mumma@nasa.gov

Published 15 January 2009 on *Science* Express
DOI: 10.1126/science.1165243

This PDF file includes:

SOM Text
Figs. S1 to S6
References and Notes

Supporting Text

SOM-1:

Our current dataset of biomarker gases extends over a period of 10 years, and was acquired primarily with two instruments: CSHELL (Cryogenic Echelle Spectrograph [1, 2]) at NASA-IRTF (Infrared Telescope Facility) and NIRSPEC (Near Infrared Spectrograph [3]) at Keck-2. The third instrument used (Phoenix spectrometer at Gemini South) suffered from internal scattered light, especially for a very bright source such as Mars; we were not able to remove that artifact fully, and so defer discussion of Phoenix data to a future publication.

Observing from a high altitude site (e.g., Mauna Kea, HI) reduces extinction by terrestrial methane, and (especially) by condensable species (H_2O and HDO). A significant wavelength shift further reduces extinction by terrestrial counterparts, and so we target Mars when its line-of-sight velocity is large (e.g., >10 km/sec when searching for CH_4).

Most of the observations were performed using CSHELL/IRTF, which features an instrumental resolving power of 40,000, a sampling rate of 100,000, and a spectral bandwidth of 7 cm^{-1} at 3000 cm^{-1}. Since the width of the Martian lines (~0.004 cm^{-1}) is much narrower than the instrumental resolution (~0.08 cm^{-1}), the observed line shapes are defined by the instrument's transfer function with a spectral width of 2 to 4 pixels (see Fig. 1 of main manuscript). The instrument is very stable in frequency, with maximum observed spectral displacements of 0.004 cm^{-1} (or 0.13 pixels) in 30 minutes. All data presented in this paper have been organized and processed in sets of 30 minutes or less, and therefore these micro-deviations do not affect the residual spectra.

We followed our standard observing methodology, orienting the spectrometer entrance slit North-South on the planet and using the narrowest available slit (0.5 x 30 arc-sec with CSHELL and 0.144 x 12 arc-sec with NIRSPEC) to maximize the spectral resolving power. The spatial scale is 0.2 arc-sec per pixel for CSHELL and 0.198 arc-sec for NIRSPEC, and both slits are longer than the planetary diameter (7 arc-sec in March 2003). We nodded each telescope along the slit in a sequence of four scans (ABBA) with an integration time of 1 minute per scan. CSHELL observations sampled Mars in both positions along the slit (A and B separated by 15 arc-sec), allowing maximum efficiency. With the shorter NIRSPEC slit, we sampled Mars only in the A position and nodded 30 arc-sec along the slit to a sky position (B). The sum (A – B – B + A) removed telluric and other parasitic emissions, presenting the Mars spectral-spatial information for further analysis. At each grating setting, flat-field and dark frames were obtained immediately afterward for data calibration purposes. The sensitivity of the resulting spectra is mainly defined by photon noise statistics. A typical 60-second Mars exposure will lead to a signal (S) of 1000 counts [ADU/pixel] on the detector, and a corresponding noise (N) equal to sqrt(S/G) = 9.5 [ADU/pixel], where G = 11 electrons/ADU (CSHELL's detector gain). A typical set of 20 minutes on source and integrated over 3 pixels along the slit, would correspond to a S/N ratio of 815 or a precision of 0.12%.

The spatial resolution of our measurements is restricted by the point-spread-function (PSF) of the observations (which is determined by the combined effects of diffraction and atmospheric seeing) and by guiding inaccuracies. To correct guiding error, exposures were processed individually and then were registered to an established fiducial position before co-addition of frames. Positioning errors due to differential refraction are minimized since these spectrometers

are designed to guide using a broadband image sampled at a comparable wavelength. To reproduce the continuum spatial profile observed along the N-S meridian, we assumed a "Lambertian" surface and included two components in the emergent intensity: reflected sunlight and thermal emission from the surface. This permitted improved alignment of the frames, and provided higher precision when pixelated spectra were mapped into latitude-longitude positions on the planet.

SOM-2:

In our early investigations (before 2005), we removed telluric absorption features by extracting the Mars spectrum at one position along the slit, and subtracting it from spectra measured at other positions. This approach worked well for water vapor. However, it significantly reduced the intensity of the residual spectral lines for well-mixed species on Mars (e.g., CO_2), and demonstrated the need to extract absolute abundances for trace species such as methane. The extraction of absolute spectral signatures is, however, extremely complex. It requires precise frequency calibration (better than ten milli-pixels), along with synthesis of the telluric transmittance at very high spectral resolution [approaching 100 m/sec (or 0.001 cm^{-1} at 3000 cm^{-1})].

Since 2005, we re-designed our spectral analysis software to achieve absolute extractions (4,5). We developed new techniques to account for instrumental effects, thereby permitting an order of magnitude increase in sensitivity in processed spectra. Our current tools include correction (with milli-pixel precision) of spatial and spectral distortions introduced by anamorphic optics in the spectrometers, removal of internal scattered-light, correction of variable resolving power (along the slit and along the dispersion direction), removal of spectral fringing (using Lomb periodogram analysis), correction of residual dark current, and correction of residual telluric radiance.

We incorporated new models for synthesizing (at sub-Doppler resolution) atmospheric transmittance on Earth and Mars that together form the basis for absolute extractions. We now compare the observed sky radiance with spectra synthesized using a rigorous line-by-line, layer-by-layer radiative transfer model of the terrestrial atmosphere (GENLN2, version 4 [6]). Several improvements were introduced to this terrestrial atmospheric model [4,7,8], and it now properly accounts for spectral pressure shifts. The molecular database accessed by the model was also updated to include the latest spectroscopic parameters [8]. In particular, recently corrected and extended parameters for H_2O and C_2H_6 species [9] were included.

Systematic uncertainty and Random errors:

Systematic uncertainty can be introduced by errors in the synthetic model for terrestrial transmittance, for example by errors in the molecular line parameters, errors in abundance of contributing chemical species (especially if omitted entirely), and errors in emission/absorption processes. It can also be introduced by electronic effects, such as print-through of clocking signals in the CCD detectors.

To remove the most significant systematic uncertainties, we formed a background spectrum (based on our 7 years of data) and removed it from the reduced spectra. The background spectrum was computed by averaging over all spectral residuals (after removing real martian lines), and it corrected systematic errors arising from uncertainties in the molecular parameters used to calculate the terrestrial transmittance spectra. The background spectrum was comparable

in intensity (standard deviation of 0.13%) to the instrumental photon noise (typically a standard deviation of 0.12%); because the background was removed from all spectra, it did not introduce spatial variations in the final spectra.

Although reduced by this approach, some systematic effects remained. In Figs. 1D & 1E, we show gray-scale images of the spectral residuals row-by-row along the slit (after removing the "background spectrum"). Remaining systematic errors can be recognized in 1D & 1E as columns that are whiter or blacker than the mean (e.g., in the range 3034.5 - 3035.6 cm^{-1}). For each row, we formed the RMS of spectral residuals and adopted this as a measure of the combined random and systematic errors in that row (we except columns containing observed or expected CH_4 and H_2O lines). We then combined the errors for the three spatial rows and three spectral columns representing the detection (shown for a given latitude bin in Fig. 2A), and we expressed the "error" as an equivalent column density. Close inspection reveals that systematic errors form a major component of the total error budget. However, systematic errors tend to be correlated from row to row, and thus do not affect the scatter amongst the points of Fig. 2A greatly.

Random errors arise mainly from stochastic noise of the (total) photon stream accumulated for each spectral extract, and the amount varies with spectral position. At spectral positions removed from strong terrestrial lines, Mars is brighter than the terrestrial foreground so it dominates the stochastic noise there. In the cores of strong terrestrial lines (CH_4, H_2O), (weaker) terrestrial emission dominates so the noise is smaller there. The actual stochastic noise at the position of Mars CH_4 lines is intermediate to these two values and it depends on the specific Doppler-shift when Mars was observed. The combined photon number is nearly independent of position along the slit, thus the 1-σ stochastic noise levels (noise-equivalent column abundance) are nearly the same for points in Fig 2A, though we reiterate that systematic error comprises the greater part of the total error budget.

In contrast with Fig. 2A, the 1-σ confidence levels (noise-equivalent mixing ratio) in Fig. 2B differ from one another, because both the two-way airmass on Mars and the topographic correction differ point-by-point along the slit.

SOM-3:

We co-measure multiple spectral lines of water vapor in both methane settings (Fig. 1B and 1C). The extracted spectra were binned over longitude ranges (Table 1) centered at the indicated CML and by 3-pixels along the slit (0.6"), but the latitudinal extent of the spectral bins differs slightly as Mars' apparent diameter changes (4.8" for profiles 'b' & 'c', 6.95" for profile 'd', and 10" for profile 'a') (Table 1). The residuals are also represented as grey-scale maps in Figs. 1D and 1E, which reveal strong latitudinal gradients for both gases. Water vapor is concentrated in the Northern hemisphere, as expected for this season (L_s = 155º, or late summer in the North). From the measured line intensities, we derived the water vapor column on Mars by using a Levenberg-Marquardt retrieval algorithm and a multi-layer planetary radiative transfer model (CODAT package) for calculating the synthetic spectra. The local atmospheric conditions (pressure and temperatures) fed to the radiative transfer model were calculated using the LMD-AOPP-IAA general circulation model [10], a non-linear, global and three-dimensional hydrodynamic model of the Martian atmosphere.

The retrieval of molecular abundances includes corrections for double path absorption (Sun-to-surface and surface-to-observer air masses) and surface thermal emission for one-way (surface-to-observer) absorption only. At these wavelengths, the radiation received from Mars is a combination of reflected-sunlight (with Fraunhofer lines) and planetary thermal emission (featureless continuum). Sparse spectral lines of Mars' atmospheric constituents are superposed on the continua according to the optical path sampled by the two components (Fig. 1).

The varied surface temperatures and albedos across the Mars surface lead to differences in the apparent thermal/solar ratio, and thus in the apparent equivalent width of the observed Fraunhofer lines. By comparing residual spectra of Mars to the solar spectrum measured by the ATMOS instrument [11,12], we estimated the ratio of the thermal and solar components pixel-by-pixel along the slit [13]. We retrieve the true vertical column density which gives rise to the observed Mars lines, by correcting for the double path atmospheric extinction of solar radiation (with appropriate incidence and viewing angles) and for one-way extinction of surface thermal emission.

We constructed a multi-layer model for Mars' atmosphere and extracted the column density (molecules cm^{-2} along the two-way path traversed by reflected sunlight, i.e., the sum of Sun-to-Mars-surface and Mars-surface-to-Earth) needed to reproduce the lines (CH_4 R1, R0; H_2O) seen in the measured spectral residuals of Figures 1B and 1C. We then calculated the zenith column density for each spatial footprint, and obtained mixing ratios by comparing our retrieved zenith column densities (CH_4, H_2O, etc.) with the CO_2 column for that footprint. We validated this approach for relevant dates (Table 1) by comparing parameters retrieved from our spectral data with those measured from Mars orbit by TES (14,15) (e.g., H_2O on UT 16 January 2006; Table 1, Fig. S4). We also compared with predictions of two General Circulation Models (10,16) tailored for the local time on Mars and using MOLA (17,18) altitudes averaged over each footprint (Fig. S3, S5). The agreement for surface pressure and temperature is within errors of the GCM data. Our extracts for H_2O also agree well with those measured by TES over the interval 15-25 March 2003 and averaged over each spatial footprint. These comparisons validate our approach and demonstrate that reliable absolute abundances are recovered. The equivalent widths of our measured methane lines are the same order of magnitude as the retrieved water lines indicating the validity of our approach for determining the absolute methane abundance.

In Fig. S6, we compare spectra for the four data sets represented in Fig. 2C. Spectral extracts for each date were averaged over latitudes 5º - 50º N, further improving the signal-to-noise ratio in the mean spectra and more clearly revealing the molecular lines (CH_4 and H_2O). These extracts reveal that individual line intensities change significantly with location on the planet and with season. The observed behavior of H_2O lines shows that atmospheric water vapor is negligible at the beginning of northern spring, but increases strongly as the surface warms and surface ices vaporize; this behavior has long been known from spacecraft and ground-based measurements (14, 19,20,21). Methane also varies greatly – we find only a suggestion of the R1 line in early spring (a), but a strong detection by early summer (b, c) and a further increase by late summer. The small mean mixing ratio (3 ± 1 ppb, over 15º N - 60º S) seen in profile 'a' (Fig. 2C) places strong constraints on models for methane release and destruction (see main text). The spectral extracts for early summer ('b' & 'c' in Fig. S6) reveal strong changes in the CH_4 R1 line with longitude, reflecting the changing abundance ratios revealed by spatial profiles for methane (profiles 'b' & 'c' in Fig. 2C).

The algorithm used to retrieve the molecular abundances was the gradient-expansion least-squares algorithm (Marquardt). This well established method combines the advantages of the gradient search for the first portion of the search and behaves more like an analytical solution as the search converges (22). It finds the solution efficiently, directly and is practically insensitive to the initial conditions.

The goodness of the fit was calculated in the standard fashion as:

$$\chi_v^2 \equiv \frac{1}{N-m}\sum\left\{\frac{1}{\sigma_i^2}\left[y_i - f(x_i)\right]^2\right\}$$

where N is the number of pixels in the spectrum, m is the number of parameters (abundances) being fitted, σ_i represents the individual uncertainty of pixel i, y_i is the residual transmittance intensity, $f(x_i)$ is the synthetic model computed using multi-layer planetary radiative transfer model (described above), and x_i is the frequency of pixel 'i'. In a perfect fit (y=f(x)), χ_v^2 is equal to 1 if the defined uncertainties (σ_i) are equal to the 'true' uncertainty of the points. Because of the selected binning of our data and quality of the residuals, we are mostly dominated by photon noise statistics, so $\sigma_i \sim$ photon noise. Nevertheless, errors in the computation of residuals will lead to additional sources of uncertainty, and for that reason we compute for each residual spectrum the 'true' standard deviation of the points (σ, which includes photon-noise error and instrumental/modeling uncertainties). Our uncertainties ($\sigma_i = \sigma$), therefore, include all quantifiable sources of intensity error, and consequently the resulting χ_v^2 is by definition equal to 1. The uncertainty of the retrieved parameters (CH_4, H_2O, CO_2 abundances) is then calculated in terms of the curvature of χ_v^2 function in the region of minimum using the standard error propagation analysis of the gradient-expansion least-squares algorithm.

Uncertainties can also be introduced by errors in the assumed atmospheric conditions. The temperature errors of the GCM are less than 5K (if compared to values retrieved by MGS/TES), while the pressure uncertainty is estimated to be lower than 0.03 mbar (23). The uncertainty in surface pressure will lead to errors of ~0.5% in abundance for a typical 6 mbar surface pressure, while a 5K error in the temperature would affect abundances retrieved from the R1 line by less than 4%. These uncertainties are smaller than those defined by the intrinsic sensitivity of measurements.

Our absolute retrievals of water vapor column densities agree well with TES data averaged over the same spatial footprints, for the latitude ranges sampled (Fig. S4). Moreover, our absolute retrievals of surface pressure and gas temperature (at the surface and in the first scale height) agree well with TES data and GCM models (Fig. S5). Together, they validate the rigor of our observational, data reduction, and analytical approaches.

SOM-4:

The mean diameter of Mars is ~ 6790 km, so a 60° arc along a great circle spans ~ 3555 km on the surface. Points that are 30° (1800 km) distant from a central locus enclose a surface area (A_s) of ~ 9.7 x 10^6 km^2), representing ~ 6.7% of Mars' entire surface area (1.45 x 10^8 km^2). The mean column density of Mars' atmosphere is ~2.2 x 10^{23} molecules cm^{-2} or ~ 0.365 mol cm^{-2}, so a trace gas with mean mixing ratio of 1 ppb then represents ~ 3.65 mol km^{-2}. At 1 ppb, A_s then contains 3.54 x10^7 moles of the trace gas.

SOM-5:

The presence of a well-defined peak in mixing ratio with latitude (e.g., near 0º N in profile 'd') coupled with (approximately equal) concentration gradients towards the North and South caused us to consider (first) steady release from a central source with radial expansion driven by the observed concentration gradients (Model 1). A simple model demonstrated that the time scale for filling the plume by Fick's diffusion is very long (~10^7 years); persistence of the plume over this long interval is required but is not supported by our observations. We next considered release from multiple individual release zones distributed over a large region, with Fickian diffusion filling the gaps between local 'hot-spots' (Model 2). The diffusion radius around a local 'hot-spot' develops at a rate ~ 10 cm yr^{-1}, so a source region with 'hot-spots' separated by a modal spacing of 5 cm would fill rapidly after seasonal turn-on and the profile would appear relatively 'smooth' after 3 months. However, such small-scale structure could never be discerned at our spatial resolution (e.g., profile 'd'). While Model 2 is not eliminated by our data, strong local gradients in the density of 'hot spots' (or a continuous zone of release) are needed to produce the observed plume properties.

We then considered release from a central source region coupled with eddy diffusion (Model 3) that is often invoked to explain rapid mixing over large spatial scales. Efficient (vertical) eddy diffusion is needed to mix methane rapidly in the first few scale heights above the surface, but (much more efficient) horizontal eddy mixing is needed to effect the large meridional and zonal size of the plume. Estimated values for the vertical eddy coefficient range widely: the mean value derived from dust profiles in the lower atmosphere was 1.1 (± 0.5) x10^6 cm^2 s^{-1} (at sunset, Phobos 2 [24]), while a recommended value of 10^7 cm^2 s^{-1} was inferred from O_2 and H_2 abundances (25) and a value larger than 10^7 cm^2 s^{-1} provided a best fit to the measured abundance of H_2O_2 (26). A value of 10^7 cm^2 s^{-1} would ensure uniform mixing over two scale heights in ~5 sols (27,28). Meridional (horizontal) mixing coefficients derived from the observed reduced enhancement of polar Argon are much larger, ~ 1.4 x 10^9 cm^2 s^{-1} in March 2003 (L_s = 155°) (29,30).

We also considered release from a polar ice that is seasonally stable (winter) but becomes unstable in early spring, releasing CH_4 and H_2O (Model 4). Seasonal streaming of CO_2 and eddy diffusion are required to explain rapid transport of water vapor from the seasonal polar cap to

mid-latitude regions (31). Entrainment of CH_4 in the CO_2-H_2O stream could explain a rapid dissemination of released methane and perhaps produce a mixing ratio profile whose peak moves southward as the season advances into mid- and then late summer. The northward gradient that develops by late summer (profile 'd') could then reflect decreasing release from the seasonal polar cap. However, the longitudinal gradients seen in our data may require corresponding longitudinal enhancements of methane sourced at high latitudes.

SOM-6:

High electric fields develop at edge gradients of individual grains, ultimately permitting electric discharges that (in dust storms) might destroy methane directly (32) and might also produce H_2O_2 through ensuing chemical reactions (33,34). If so produced, H_2O_2 then could condense onto airborne grains where CH_4 could react with it, producing the principal oxidation products methanol (CH_3OH) and formaldehyde (H_2CO) (these species have short photochemical lifetimes on Mars and are rapidly removed).

Supporting Figures:

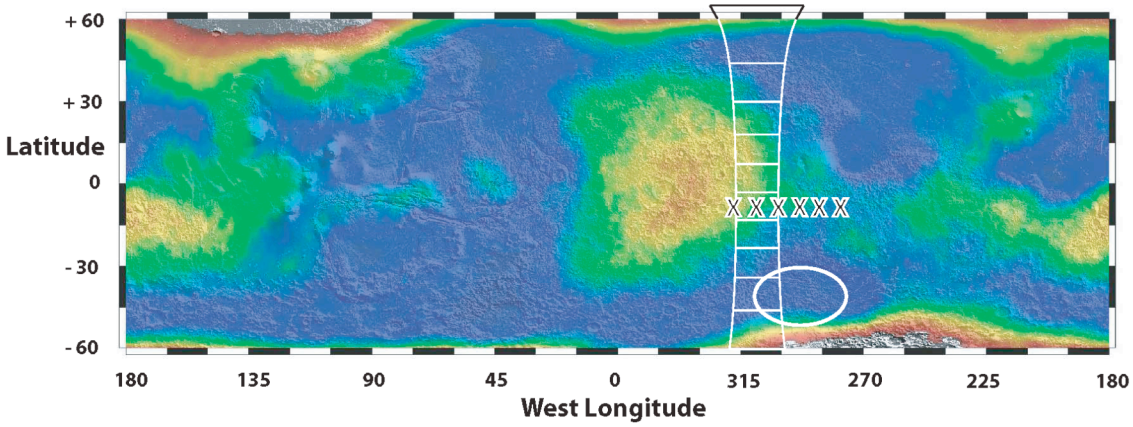


Figure S1: Spatial footprints for spectral extracts are shown projected onto a latitude-longitude map of Mars (West longitude system). We used the narrowest CSHELL slit (0.5" wide) to obtain the highest possible spectral and spatial resolution. On UT 20 March 2003, the slit width projected onto the planet (6.95" diameter) represented 448.5 km (E-W), or 8.24° longitude at the sub-Earth point. The CML advances at a rate of 14.6° degrees per hour, so the slit edges traverse a range of longitudes 15.54° in 30 minutes. Each pixel extends 0.2" along the slit (N-S), so a 3-pixel spectral extract projects onto 586 km (N-S), or 9.87° of latitude at the sub-Earth point. The footprints for 10 spectral bins (CML 310° W, 30 minutes elapsed time) are outlined in white, and the CMLs of successive extracts are marked (X) at 30-minute intervals. The 11 spectra shown in Fig. 1 are binned over 190 minutes elapsed time and thus represent a footprint 3215 km x 586 km at the sub-Earth point. Profile 'd' (Fig. 2C) represents spectra centered at CML 310°, and binned over 30 minutes. The rim of the Hellas impact basin is shown as a white oval, and the sub-surface hydrogen abundance is color-coded, for comparison [35].

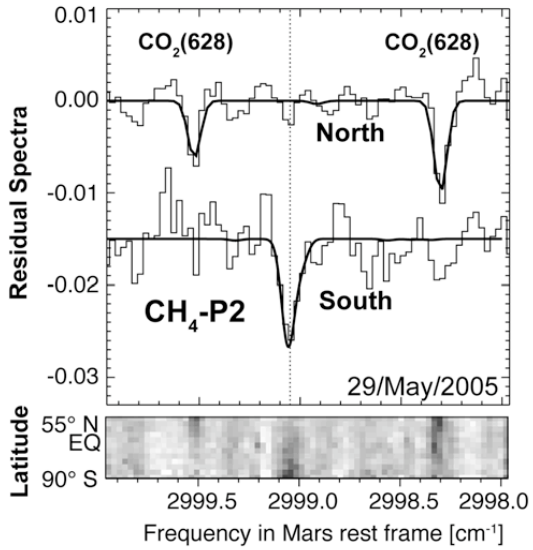


Figure S2: Detection of the CH_4 P2 doublet of the ν_3 band (consisting of lines of the E and F nuclear spin species) in May 2005 (L_s = 220°). Two lines of a newly discovered band (ν_2 + ν_3) of $^{16}O^{12}C^{18}O$ (628) are seen in the northern hemisphere (4). The CO_2 lines are stronger at high atmospheric temperature. The dark solid lines are simulated spectra.

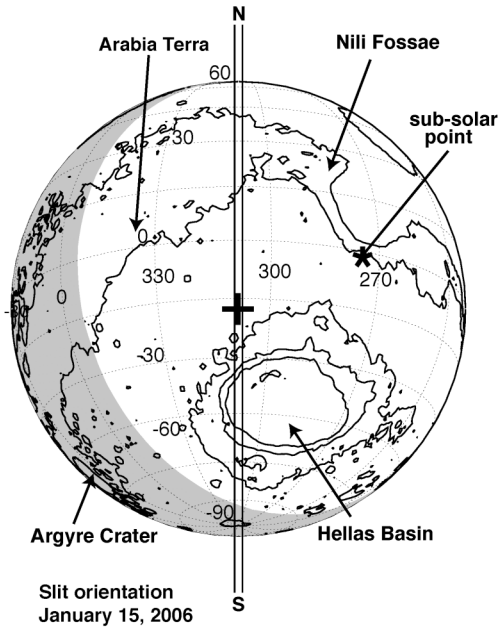


Figure S3. The aspect of Mars as seen from Earth on UT 16 January 2006 (L_s = 357°). The apparent diameter was 10 arc-seconds, and the sub-solar point is indicated. The NIRSPEC entrance slit is positioned along the central meridian longitude. Spectra were acquired at intervals of 0.2 arc-seconds along the slit, and binned to 0.6 arc-second intervals. Contours of constant altitude are shown at intervals of 3 km.

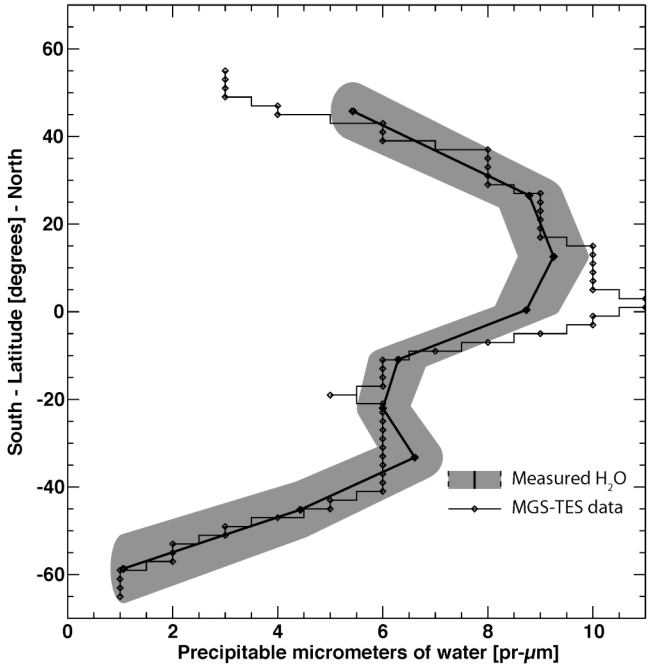


Figure S4. The column density of H_2O retrieved from NIRSPEC binned spectra (full line) is compared with measurements obtained by TES (14) on the MGS orbiter for this season (points, histogram). Diurnal differences between our measurements at 10:00 and the MGS-TES at 14:00 were reconciled by multiplying our values by 1.25. The NIRSPEC and TES results agree well with a high correlation of 96%.

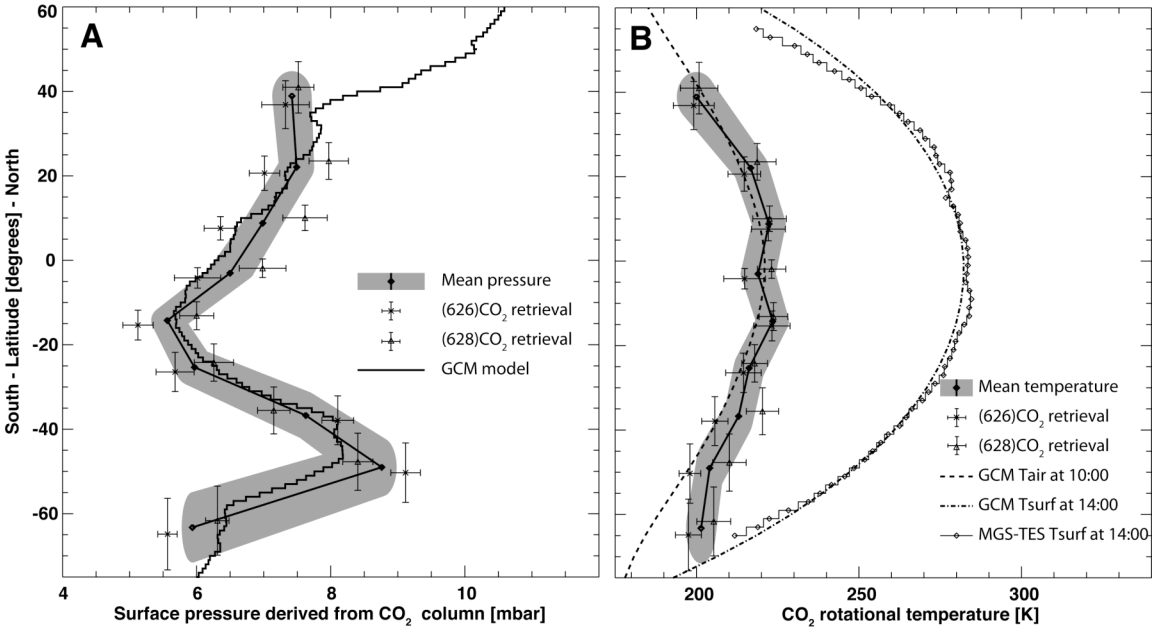
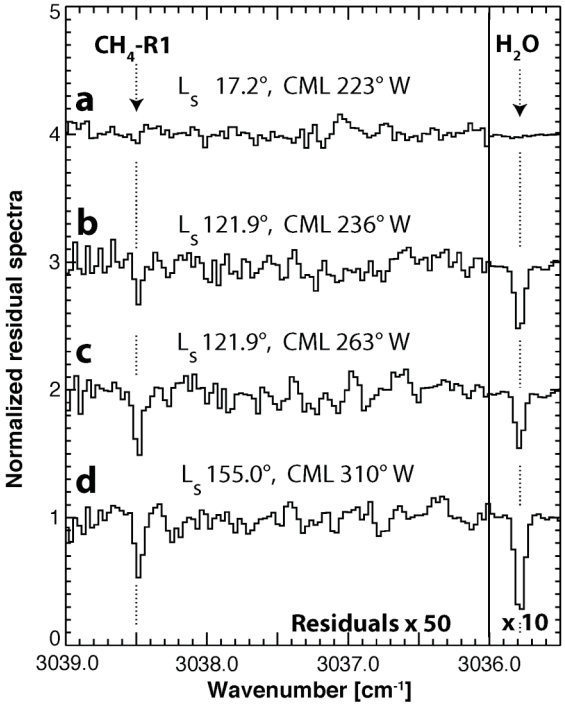


Figure S5. Retrieval of atmospheric pressure and temperature on Mars from vibrational bands of two CO_2 isotopes (626 = $^{16}O^{12}C^{16}O$; 628 = $^{16}O^{12}C^{18}O$) measured with NIRSPEC at Keck-2. The spectra were taken on 16 January 2006 and the slit was oriented N-S along the central meridian longitude (CML 290° West). We retrieved the surface pressure and temperature by using a Levenberg-Marquardt non-linear-minimization algorithm and a Martian radiative transfer model. The data reveal high-temperatures at equatorial regions as predicted by the MAOAM-GCM model [16] for this season (panel B), and they sample the high atmospheric pressure of the deep Hellas basin (panel A, 42°-- S).

Figure S6. Geographic and temporal variability of methane and water on Mars. These extracts are taken from spectra centered at the indicated longitude (CML), and binned over 30 minutes in time. The sub-Earth footprints span longitude-latitude ranges with these physical dimensions: **a:** 770 km x 535 km, **b, c:** 1274 km x 818 km, **d:** 948 km x 586 km (Table 1). We then averaged the spectra over 5 - 50° N latitude to better reveal major changes in line intensity for methane and water vapor with location on the planet and with local season, reflecting the changing abundance ratios. Mixing ratios for methane (before latitudinal binning) are shown in Fig. 2C.



References and Notes for Supplementary material

1. A. T. Tokunaga, D. W. Toomey, J. Carr, D. N. B. Hall, H. W. Epps, in *Instrumentation in Astronomy VII*, D. Crawford, Ed., *Proc. SPIE* **1235**, part 2, 131-143 (1990).
2. T. P. Greene, A. T. Tokunaga, D. W. Toomey, J. S. Carr, In *Proc. SPIE* **1946**, 311-324 (1993).
3. I. S. McLean *et al.*, in *Infrared Astronomical Instrumentation*, A. M. Fowler, Ed., (SPIE Conf. Proc. 3354), 566 (1998).
4. G. L. Villanueva, M. J. Mumma, R. E. Novak, T. Hewagama, *Icarus* **195**, 34 (2008).
5. G. L. Villanueva, M. J. Mumma, R. E. Novak, T. Hewagama, *J. Quant. Spectrosc. Rad. Transf.* **109** (No. 6), 883 (2008).
6. D. P. Edwards, NCAR Tech. Note NCAR/TN-367+STR (1992).
7. T. Hewagama *et al.*, *Proc. SPIE* **4860**, 381 (2003).
8. T. Hewagama *et al.*, *J. Quant. Spectr. Rad. Transf.,* **109**, 1081 (2008).
9. L. S. Rothman *et al.*, *J. Quant. Spectr. Rad. Tran.* **96** (2), 139 (2005).
10. F. Forget *et al., J. Geophys. Res.* **104** (E10), 24155 (1999).
11. C. B. Farmer, in *Infrared Solar Physics*, D. M. Rabin *et al.*, Eds. (IAU- Netherlands 1994), 511.
12. C. B. Farmer, R. W. Norton, in *A High Resolution Atlas of the Infrared Spectrum of the Sun and The Earth Atmosphere from Space, Vol. I: The Sun* (NASA Ref. Pub. 1224, vol. 1, Washington, DC, 1989).
13. R. E. Novak, M. J. Mumma, M. A. DiSanti, N. Dello Russo, K. Magee-Sauer, *Icarus* **158** (1), 14 (2002).
14. The Thermal Emission Spectrometer (TES) is carried on the Mars Global Surveyor spacecraft orbiting Mars (15); it provided detailed maps of H_2O, temperatures, and aerosols on Mars. We compare with updated H_2O values.
15. M. D. Smith, *Icarus* **167**, 148 (2004).
16. G. L. Villanueva, PhD thesis, Copernicus Verlag, ISBN 3-936586-34-9 (2004).
17. The Mars Observer Laser Altimeter (MOLA) is carried on the Mars Global Surveyor spacecraft orbiting Mars; it provided detailed maps of local altitudes relative to the mean geoid of Mars (18).
18. D. E. Smith *et al.*, *J. Geophys. Res.* **106** (E10), 23689 (2001).
19. A. L. Sprague *et al.*, *Icarus* **184**, 372 (2006).
20. B. M. Jakosky, R. M. Haberle, in *Mars*, H. H. Kieffer *et al.*, Eds. (Univ. Ariz. Press, Tucson, 1992).
21. B. J. Conrath *et al., J. Geophys. Res.* **78**, 4267 (1973).
22. P. R. Bevington and D. K. Robinson, *Data Reduction and Error Analysis for the Physical Sciences* (McGraw-Hill, New York 1992) ISBN 0-07-911243-9.
23. F. Forget *et al.*, *J. Geophys. Res.* **112**, E08S15 (2007).
24. O. I. Korablev, V. A. Krasnopolsky, A. V. Rodin, *Icarus* **102**, 76 (1993).
25. J. Rosenqvist, E. Chassefiere, *J. Geophys. Res.* **100** (No. E3), 5541 (1995).
26. Th. Encrenaz *et al., Astron. Astrophys.* **396**, 1037 (2002).
27. Mars' sidereal rotation period (at the equator) defines the sol (24.62 hr).
28. D. M. Hunten, in *Mars Atmosphere Modeling and Observations*, F. Forget *et al.*, Eds. (ESA, Noordwijk, 2006), 415.
29. S. M. Nelli *et al.*, *J. Geophys. Res.* **112**, E08S91 (August 2007).
30. A. L. Sprague *et al.*, *Science* **306**, 1364 (2004).
31. M. A. Mischna, M. I. Richardson, R. J. Wilson, D. J. McCleese, *J. Geophys. Res.* **108** (E6), 5062, 16-1 (2003).
32. W. M. Farrell, G. T. Delory, S. K. Atreya, *Geophys. Res. Lett.* **33**, L21203 (2006).
33. S. K. Atreya *et al., Astrobiology* **6** (3), 439 (2006).
34. G. T. Delory *et al.*, *Astrobiology* **6** (3), 451 (2006).
35. W. C. Feldman *et al., J. Geophys. Res. (Planets)* **109** (E9), IDE09006 (2004).